

New Global Potential Energy Surfaces of the ground $^3A'$ and $^3A''$ states of the H_2O system

Alexandre Zanchet,^{1, a)} Marta Menéndez,^{2, b)} Pablo G. Jambrina,^{3, c)} and F. Javier Aoiz^{4, d)}

¹⁾Departamento de Química Física I, Facultad de Ciencias Químicas, Universidad Complutense de Madrid, 28040 Madrid, Spain

Departamento de Química Física, Facultad de Ciencias Químicas, Universidad de Salamanca, 37008 Salamanca, Spain

²⁾Departamento de Química Física I, Facultad de Ciencias Químicas, Universidad Complutense de Madrid, 28040 Madrid, Spain

³⁾Departamento de Química Física, Facultad de Ciencias Químicas, Universidad de Salamanca, 37008 Salamanca, Spain

⁴⁾Departamento de Química Física I, Facultad de Ciencias Químicas, Universidad Complutense de Madrid, 28040 Madrid, Spain

(Dated: 5 June 2019)

This paper presents two new adiabatic, global potential energy surfaces (PESs) for the two lowest $^3A'$ and $^3A''$ electronic states of the $O(^3P)+H_2$ system. For each of these states, *ab initio* electronic energies were calculated for more than 5000 geometries using internally contracted multireference configuration interaction methods. The calculated points were then fitted using the ansatz by Aguado *et al.* [Comput. Phys. Commun. **108**, 259 (1998)] leading to very accurate analytical potentials well adapted to perform reaction dynamics studies. Overall, the topographies of both PESs are in good agreement with the benchmark potentials of Rogers *et al.*, but those presented in this work reproduce better the height and degeneracy of the two states at the saddle point. Moreover, the long range potential in the entrance channel does not require any cutoff. These features makes the new PESs particularly suitable for a comparison of the dynamics on each of them. The new set of PESs were then used to perform quantum mechanics and quasiclassical trajectory calculations to determine integral and differential cross sections, which are compared to the experimental measurements by Garton *et al.* [J. Chem. Phys., **118**, 1585 (2003)].

I. INTRODUCTION

The $O(^3P) + H_2 \rightarrow OH(^2\Pi) + H$ reaction has received a great deal of attention over the last 60 years due to its importance in combustion of hydrogen and hydrocarbons, where it plays a key role in chain branching and propagation,^{1,2} and in atmospheric reactions in the upper atmosphere³. It is also one of the most important reactions in shocked interstellar clouds⁴ and in protoplanetary disks.⁵ Consequently, there has been a long series of measurements of thermal rate coefficients (see Ref. 6 and references therein).

Although its detailed dynamics had been subject of numerous theoretical studies,^{7–16} experimental studies on the title reaction are scarce due to the large electronic barrier of the reaction, requiring $O(^3P)$ atoms to be accelerated to hyperthermal energies in a $O(^1D)$ -free atomic beam. Particularly relevant for the reaction dynamics community are the experiments carried out by Minton and coworkers,^{17–20} where they used a crossed-molecular beam machine coupled with a hyperthermal atomic-oxygen beam source and laser-induced fluorescence detection to determine the excitation func-

tion, the collision energy dependence of the integral cross section (ICS),¹⁷ differential cross sections (DCS),¹⁸ and rotational energy distributions^{18–20} using laser induced fluorescence with a resolution capable to determine the non-statistical Λ -doublet population ratio of the nascent $OH(^2\Pi)$ as a function of the OH vibrorotational state.^{19,20}

Omitting the spin-orbit splitting, there are three potential energy surfaces (PES) that correlate with the reactants in their ground states, $O(^3P_g) + H_2(^1\Sigma_g^+)$; two of them, of symmetries $^3A'$ and $^3A''$, also correlate adiabatically with the ground state products, $OH(^2\Pi)+H(^2S)$. These two PESs are degenerate for collinear geometries resulting from the Π character of the linear arrangement of the three atoms. Given the fact that *ab-initio* calculations for both PESs systematically predict a collinear saddle point with a barrier height close to 0.6 eV, one would expect similar reactivities on the two PESs, at least at low collision energies. However, as reactants move apart from a collinear geometry, the barrier height rises more sharply in the case of the $^3A'$ state, which explains why $^3A''$ PES exhibits a larger reactivity. Of all the existing PESs available in the literature, those calculated by Rogers *et al.*⁹ (hereinafter RWKW PESs) have been widely used in dynamical and kinetic computational studies for the title reaction and they are supposed to be the most accurate PESs to this moment. As such, they can be considered as benchmark PESs for the title reaction.

^{a)}azanchet@ucm.es

^{b)}menendez@quim.ucm.es

^{c)}pjambrina@usal.es

^{d)}aoiz@quim.ucm.es

In this article we primarily present the computational details of a new pair of global ${}^3A'$ and ${}^3A''$ PESs which have been recently used to determine the Λ -doublet populations of the produced OH(X).²¹ High-level *ab initio* calculations have been fitted to a convenient ansatz that includes analytical gradients, making them very efficient to perform classical and semi-classical reaction dynamics treatments. In fact, the collinear barrier, and most of the minimum energy path, of the analytical PESs are virtually identical, in contrast to previous sets of PESs.⁹

This work is structured as follow. Section II is devoted to the description of the theoretical approaches, the details on the *ab initio* calculations are found in section II A, the fitting procedure is described in section II B and the reaction dynamics calculations are presented in section II C. The results are discussed in section III before the conclusions in section IV.

II. THEORETICAL METHODS

A. Ab initio calculations

Ab initio calculations were performed over the configuration space of the OHH system to build analytical PESs of the two lowest ${}^3A'$ and ${}^3A''$ states. All calculations were done using the MOLPRO suite of programs.^{22,23} For both oxygen and hydrogen atoms, Dunning's aug-cc-pV5Z basis set²⁴ including *spdfg* basis functions were used. Both states correlate with both ground state asymptotic channels $O({}^3P)+H_2$ and $OH({}^2\Pi)+H({}^2S)$, where they are degenerate when spin-orbit effects are not considered. To get an accurate and homogeneous description of both PESs, the state-average complete active space (SA-CASSCF) method²⁵ was employed to calculate the first ${}^3A'$ and the two first ${}^3A''$ electronic states. The active space considered consists in 8 electrons distributed in 6 orbitals (2-6 a' and 1 a'') to include all valence orbitals of oxygen and the 1s orbitals from both hydrogen atoms. The resulting state-average orbitals and multireference configurations were then used to calculate both the lowest ${}^3A'$ and the lowest ${}^3A''$ states energies with the internally contracted multireference configuration interaction method (icMRCI) including simple and double excitations²⁶ and Davidson correction.²⁷ The 1s orbital of oxygen was kept frozen throughout the calculations.

To get a good description over the configuration space, the *ab initio* points were sampled using the Jacobi coordinates (r, R, γ) , where, for a triatomic system $A+BC$, $\mathbf{r} = R_{BC}$, \mathbf{R} is the vector from the atom A to the center of mass of the diatomic BC, and γ is the angle between \mathbf{r} and \mathbf{R} . Taking advantage of the symmetry of the system, a first set of points have been calculated on a three-dimensional regular grid $(N_r=18) \times (N_R=26) \times (N_\gamma=10)$ on the $O+H_2$ Jacobi coordinates, with $(0.7 \leq r \leq 4.9) a_0$, $(0.1 \leq R \leq 10) a_0$ and $(0 \leq \gamma \leq 90)$ degrees. To improve the description of long range interactions in the $O+H_2$ channel, 20 values of R ($5 \leq R \leq$

10) a_0 have been added to the grid when $(1 \leq r \leq 2) a_0$. Finally, a last set of points have been calculated on a three-dimensional grid $(N_r=5) \times (N_R=14) \times (N_\gamma=7)$ based on the $H+OH$ Jacobi coordinates to refine the description of this asymptotic channel, with $(1.6 \leq r \leq 2.4) a_0$, $(2 \leq R \leq 5) a.u.$ and $(0 \leq \gamma \leq 180)$ degrees. Overall, excluding non-converged points, there have been calculated ≈ 5000 *ab initio* energies for each of the two PESs sampled over all the configuration space. To complete the description, *ab initio* calculations were also performed to describe the OH and H_2 diatomic potential energy curves considering 40 and 52 points respectively.

B. Fitting Procedure

The *ab initio* icMRCI+Q energies for the electronic states ${}^3A'$ and ${}^3A''$, have been fitted separately using the GFIT3C procedure introduced in Refs.²⁸⁻³⁰, in which the global PES is represented by a many-body expansion:

$$V_{ABC} = \sum_A V_A^{(1)} + \sum_{AB} V_{AB}^{(2)}(R_{AB}) + V_{ABC}^{(3)}(R_{AB}, R_{AC}, R_{BC}), \quad (1)$$

where $V_A^{(1)}$ represents the energy of the atoms ($A=O, H, H$) in the ground electronic state, $V_{AB}^{(2)}$ the diatomic terms ($AB=OH, OH, HH$) and $V_{ABC}^{(3)}$ the 3-body term ($ABC=OHH$).

The diatomic terms can be represented by a sum of short- and long-range contributions. The short-range potential is defined as a shielded Coulomb potential, whereas the long-range term is a linear combination of modified Rydberg functions defined as:³¹

$$\rho_{AB}(R_{AB}) = R_{AB} \exp \left[-\beta_{AB}^{(2)} R_{AB} \right], \quad AB = OH, OH, HH \quad (2)$$

with $\beta_{AB}^{(2)} > 0$. The root-mean-square (rms) error of the fitted diatomic potentials compared to the *ab initio* values are 4.0 and 1.7 meV for OH and H_2 , respectively. In a similar way, the 3-body term can also be expressed as an expansion of modified Rydberg functions:

$$V_{ABC}^{(3)}(R_{AB}, R_{AC}, R_{BC}) = \sum_{ijk}^K d_{ijk} \rho_{AB}^i \rho_{AC}^j \rho_{BC}^k \quad (3)$$

This fitting procedure has the advantage of being fast in the evaluation of both the potential and its analytical derivatives. Since symmetry of the system can be implicitly included, GFIT3C is well adapted to fitting triatomic systems involving H_2 ³²⁻³⁵. This property arises because for ABB systems there are only two non linear parameters to be considered, β_{OH} and β_{HH} in the present case, which can be coupled to additional constraints in the linear parameters d_{ijk} to ensure symmetry of the PES with respect to the permutation of the two H atoms, and thus reducing the number of parameters to be evaluated.²⁸⁻³⁰ The linear parameters d_{ijk} (with $i + j + k \leq L$) and the

two nonlinear parameters β_{OH} and β_{HH} , are determined by fitting the calculated *ab initio* energies after the subtraction of the one- and two-body contributions. In the present case, the order of the developmental L was taken equal to 10 for both states. One of the requirement of the three-body term is that it vanishes when one of the internuclear distances reach infinity, but it can reach high values for short distances. If the energy variation is too large, the fitting procedure tends to produce oscillations due to the high degree of the polynomial chosen, leading to an unphysical description of the long-range behavior which is required to be smooth. To avoid this problem, *ab initio* points with high energies corresponding to geometries in the repulsive part of the PES or near the total dissociation region have been excluded without significant loss of precision as these regions are well described by the sum of diatomic potentials. Finally, considering only 3400 and 3300 points (energies below 2.8 eV), an average rms error of 11.7 meV (94 cm^{-1}) and 10.1 meV (81.5 cm^{-1}) have been obtained for the $^3A'$ and $^3A''$ states, respectively.

C. Dynamical Calculations

We have carried out time independent QM calculations on the PESs presented here using the close-coupled hyperspherical method devised by Skouteris *et al.*³⁶ The results were obtained for a grid of 60 energies from $E_{\text{tot}} = 0.45$ eV to $E_{\text{tot}} = 2.5$ eV for both parities of the incoming H_2 molecule and the triatomic system. The basis set included all diatomic energy levels to $E_{\text{max}} = 3.25$ eV. The propagation was carried out in 300 log-derivative sectors until reaching a maximum hyperradius of $15 a_0$ where the matching to product states is carried out. Total angular momenta and up to 50 (62 at $E_{\text{tot}} > 1.5$ eV). Helicities up to 15 and 24 have been included in the calculations on the A' and on the A'' PESs, respectively.

Quasiclassical trajectories(QCT) were run using the procedure described in Refs. 37,38. The excitation function was calculated by running batches of 10^6 trajectories for each H_2 rovibrational state considered in this work. For each batch, the collision energy was varied continuously between 0.35 and 2.0 eV. The trajectories were started at a atom-diatom distance of 10 \AA using an integration step of 3×10^{-17} s which guarantees a total energy conservation better than one part in 10^5 .

III. RESULTS AND DISCUSSION

A. Potential energy surface

As starting point, the diatomic potential curves for OH and H_2 are shown in Fig. 1. The *ab initio* points are also included in the figure as open circles to appraise the quality of the analytical fits corresponding to the two-body terms. The main spectroscopic constants of

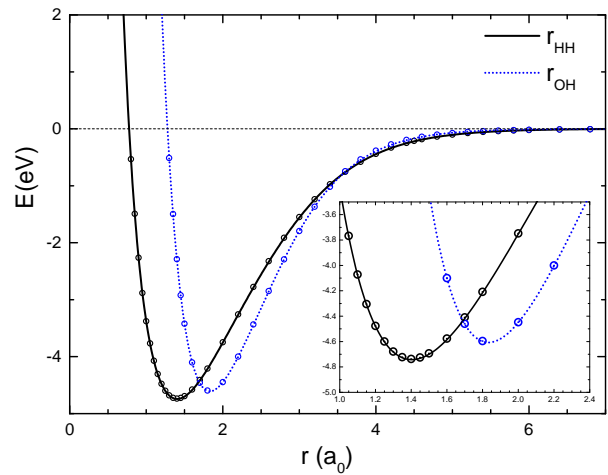


FIG. 1. Analytical potential energy curves for the asymptotic H_2 (black line) and OH (blue line). Energies refer to the respective dissociation in the ground state atoms. The circles along the curves correspond to the *ab initio* results to assess the quality of the two-body fits.

each diatom in their ground states are shown in Table I, where they are compared with the experimental values. In particular, the experimental dissociation energies are very well reproduced by the theoretical results. Using the diatomic potential curves, the rovibrational energies have been calculated including all states below 3.25 eV total energy. These data have been fitted to Dunham expansions, and the resulting spectroscopic parameters are compared with the experimental data. The agreement is excellent for $\tilde{\nu}_e$, B_e and is fairly approximate for the anharmonicity constants, considering that the experimental results are determined for a restricted set of rovibrational states and that they do not include the Y_{00} term.

	H_2		OH	
	Theor.	Exp.	Theor.	Exp.
D_e	4.742	4.7483	4.607	4.5791
D_0^0	4.473	4.4781	4.376	4.392
r_e	1.403	1.4011	1.832	1.832
$\tilde{\nu}_e$	4400.71	4401.21	3783.24	3737.76
$\tilde{\nu}_e x_e$	114.26	121.336	110.02	84.88
$\tilde{\nu}_e y_e$	-1.54	0.81	4.90	0.54
B_e	60.33	60.87	18.89	18.91

TABLE I. Constants of the diatomic molecules. D_e and D_0^0 in eV; r_e in a_0 ; $\tilde{\nu}_e$, $\tilde{\nu}_e x_e$, $\tilde{\nu}_e y_e$ and B_e in cm^{-1} . Theor., present work; Exp., from Ref. 39

Since we are interested in $\text{O}+\text{H}_2$ collisions, the asymptotic energy of this channel is taken as our zero reference energy. The main characteristics of the two triplet states considered in this work are: (i) the absence of deep well able to stabilize the triatomic complex, and (ii) the presence of two saddle-points (see Table II). The lower saddle-point corresponds to a linear O-H-H geom-

etry where both states are degenerate. *Ab initio* calculations locate the saddle-point at $R_{\text{OH}}=2.301 a_0$ and $R_{\text{HH}}=1.681 a_0$ with an energy of 0.591 eV above entrance channel. It is thus the main reaction barrier, located in the entrance channel of the O+H₂ collision, and identical for both states. The fitted A'' and A' analytical PESs reproduce the *ab initio* saddle-point with very good accuracy and the degeneracy is accounted for almost exactly. The saddle-point on the A'' analytical PES is found at $R_{\text{OH}} = 2.299 a_0$ and $R_{\text{HH}}= 1.681 a_0$ with an energy of +0.597 eV above the O+H₂ channel, while on the A' analytical PES, it is found at $R_{\text{OH}} = 2.295 a_0$ and $R_{\text{HH}}= 1.676 a_0$ with an energy of +0.597 eV. For comparison purposes, this saddle point in the RWKW PESs is at $R_{\text{OH}} = 2.300 a_0$ and $R_{\text{HH}}= 1.706 a_0$ with an energy of +0.565 eV for the A'' state and $R_{\text{OH}} = 2.310 a.u.$ and $R_{\text{HH}}= 1.705 a_0$ with an energy of +0.573 eV for the A' state. Hence, our global analytical PESs overestimates the *ab initio* barrier height slightly, by 6 meV for both the A'' and A' states, while the RWKW PES underestimates the barrier by 26 and 18 meV, respectively.⁹

The second saddle-point is found at higher-energy for a linear H-O-H geometry, and is also common to both states. The *ab initio* saddle-point is found for both OH distances equal to $2.248 a_0$ and lies at +1.648 eV, as indicated in Table II. Our analytical fits reproduce the *ab initio* values well, as the saddle-point is found for $R_{\text{OH}} = 2.250 a_0$ and $R_{\text{OH}} = 2.239 a_0$ for the A'' and A' states, with 1.639 eV and +1.633 eV energies, respectively. For comparison with the RWKW PES, the corresponding values are $R_{\text{OH}} = 2.246 a_0$ and $2.227 a_0$, with energies of +1.597 eV and +1.590 eV for A'' and A' states, respectively. The present and RWKW PESs are thus in good agreement for the description of the key regions of the potential, although our PESs reproduce better the *ab initio* values and, moreover, the degeneration of the two PESs for the collinear configurations.

Although none of the A' and A'' PESs feature deep wells able to form a stable complex, both display shallow van der Waals (vdW) wells in the O+H₂ entrance channel, which are nearly isotropic with respect to the O-HH orientation. For the A'' PES, the minimum of the vdW well is found for a T-shape geometry while on the A' PES, a linear configuration is preferred. Figure 2 shows the entrance channel potential topography of the vdW wells (in green) as polar R_X, R_Y plot. As shown in Table III, the location of the wells and their depths are reasonably reproduced in the fitted PES when compared with the *ab initio* results. It is interesting to point out that the A'' features a slightly deeper well even at linear geometries.

This difference in linear configuration between the two states is due to fact that in the long range region where the wells appear, the $^3\Sigma^-$ state is lower in energy than the $^3\Pi$ state, as can be seen in Fig. 3. For R_{H_2} at its equilibrium distance ($1.4 a_0$), both states cross at $R \approx 5.5 a_0$, leading to a conical intersection associated to Renner-Teller couplings. Since in this work we are

OHH			
	A'	A''	<i>ab initio</i>
$R_{\text{HH}} (a_0)$	1.676	1.681	1.682
$R_{\text{OH}} (a_0)$	2.295	2.299	2.301
Energy (eV)	0.597	0.597	0.591
Stretching (cm^{-1})	1756.6	1763.3	
Degenerate Bending (cm^{-1})	789.3	460.8	
Stretching (cm^{-1})	1824.1 <i>i</i>	1810.9 <i>i</i>	
ZPE (eV)	0.207	0.167	
Energy+ZPE (eV)	0.804	0.764	
HOH			
$R_{\text{OH}} (a_0)$	2.239	2.240	2.248
Energy (eV)	1.633	1.639	1.648

TABLE II. Location and energies of the degenerated saddle-points for the two analytical PESs compared with the optimized *ab initio* values. The energy is given relative to the O+H₂ asymptotic channel. The harmonic frequencies of the collinear saddle points and the resulting zero point energy (ZPE) are also given for both analytical PESs. The bottom part of the Table correspond to the secondary H-O-H linear saddle point.

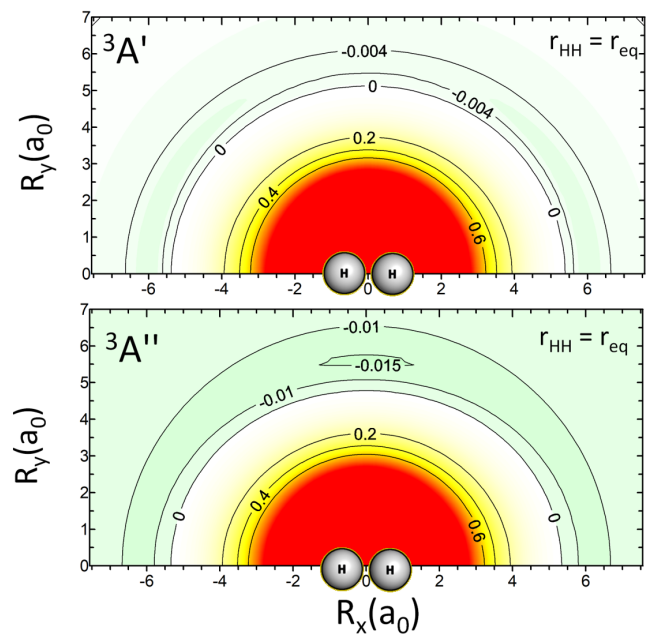


FIG. 2. Polar plot representation of the entrance channel for H₂ at its equilibrium distance, $R_{\text{H-H}} = 1.4 a_0$. The H₂ molecule lies along the x -axis with its center in (0,0). Top panel corresponds to A' state and bottom panel to A'' state.

interested in the construction of analytical PESs of the adiabatic states, Renner-Teller couplings were not studied in detail and the conical intersection is smoothed by the fitting procedure so that the resulting PESs were exempt of singularities. For larger distances, $^3\Sigma^-$ state (correlating to A'' in C_s symmetry) is more stable and thus the A'' state is lower in energy than A' . In

contrast, for shorter distances (near the saddle-point), the $^3\Pi$ state is lower in energy and both A' and A'' states become strictly degenerate in linear configuration. We should remark here that this long range region, where $^3\Sigma^-$ is the ground state, was not included in the RWKW PES, and the description of this region is one of the major difference between the present set of PESs and those from Ref. 9. This difference in the entrance channel of both states may have significant effect for inelastic collisions at low energies.

In the OH channel, both states present two degenerate VdW wells in linear configuration. The H-OH well lies at an energy of 117 meV above the O+H₂ channel in the *ab initio* calculation (depth of -18 meV with respect to H+OH asymptote) and corresponds to a linear configuration for OH distances of 1.833 a_0 and 6.011 a_0 (see Table III). The fit of the A'' PES reproduces this well, but overestimating its lying energy by 27 meV, while the fit of the A' PES exhibits no minimum for this configuration. This is the only feature that it is not well described by the new set of PESs. For the H-HO well, both fits reproduce accurately the vdW wells arising for OH distance of 1.835 a_0 and HH distance of 4.299 a_0 lying at -14 meV below the OH+H channel.

O-HH				
	A'		A''	
	Fit	<i>ab initio</i>	Fit	<i>ab initio</i>
$r(a_0)$	1.401	1.402	1.401	1.403
$R(a_0)$	5.741	5.762	5.620	5.553
$\gamma(\text{deg.})$	90	90	90	90
Energy (eV)	-0.005	-0.009	-0.015	-0.013
O-HH linear				
$R_{HH}(a_0)$	1.402	1.401	1.403	1.402
$R_{OH}(a_0)$	6.002	5.592	6.160	5.630
Energy (eV)	-0.006	-0.006	-0.012	-0.013
H-OH				
$R_{HH}(a_0)$	-	7.844	7.755	7.844
$R_{OH}(a_0)$	-	1.833	1.832	1.833
$\widehat{HOH}(\text{°})$	-	180	180	180
Energy (eV)	-	0.117	0.131	0.117
	-	(-0.018)	(-0.004)	(-0.018)
H-HO				
$R_{HH}(a_0)$	4.340	4.299	4.305	4.299
$R_{OH}(a_0)$	1.834	1.835	1.834	1.835
$\widehat{HHO}(\text{°})$	180	180	180	180
Energy (eV)	0.121(6)	0.121	0.121(4)	0.121
	(-0.013)	(-0.014)	(-0.013)	(-0.014)

TABLE III. Characteristics of the Van der Waals wells of two analytical PESs compared with the optimized *ab initio* values. Energies are given relative to the O+H₂ asymptotic channel, and for completeness, energies relative to the OH+H asymptote are given in parenthesis for the H-OH Van der Waals well.

If the system is kept at a linear configuration, where the reaction barrier is lowest, the Minimum Energy Paths

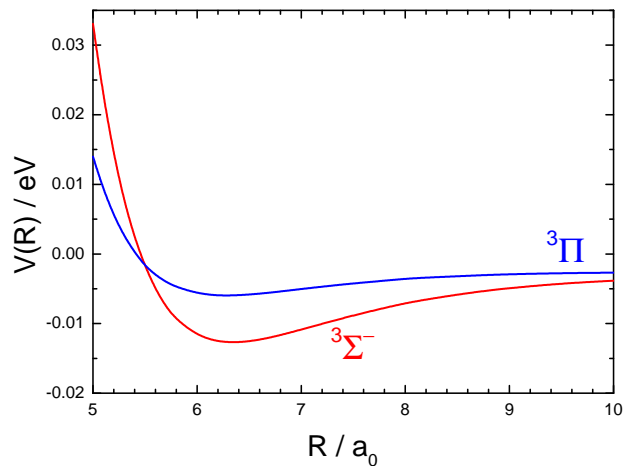


FIG. 3. Potential energy curve representing the $^3\Sigma^-$ and $^3\Pi$ diabats as a function of Jacobi vector \mathbf{R} in the linear configuration for H₂ at its equilibrium distance, $R_{HH}=1.4 a_0$

(MEPs) of the A' and A'' fits, shown in Fig. 4, are almost identical since both states are degenerate in the region of the saddle point. There is, however a perceptible difference in the entrance channel due to the crossing between the Σ^- and Π states mentioned previously. The MEPs calculated on the present PESs are very similar to those obtained using the RWKW PES (bottom panel of Fig. 4), albeit with some appreciable differences. As shown in the insets of Fig. 4, where the respective transition state regions are highlighted, the barrier is slightly higher on the present PESs, and it is in an almost perfect agreement with the *ab initio* values. In addition, the A' and the A'' degeneracy in the whole region of the collinear transition state is extremely well preserved in the present analytical PESs. In contrast, the barrier on the RWKW A' lies higher than on the A'' and the location of the transition state is slightly shifted towards the entrance channel on the former. Clearly, the present PESs are thus more precise to study the comparative reactivity on the A' and A'' PESs.

As the system draws away from the linear configuration, the degeneracy is broken and hence the overall reactivity as well as other dynamical magnitudes are expected to differ. Figure 5 depicts the bending potential (the height of the barrier as a function of the OHH angle) for the pair of PESs. As can be seen, the A' bending potential is considerably steeper than that of the A'' PES, leading to a narrower cone of acceptance and, as it will be shown, to a smaller reactivity. As a consequence of the steeper bending potential on the A' PES, the bending frequency on the A' is about a 70% larger than on the A'' whereas, as expected, the transition state symmetric stretch frequency is the same on both PESs, as shown in Table II. Therefore, the vibrational adiabatic potential (including the ZPE) is 40 meV higher on the A' PES, and this may have some repercussion on the reaction threshold on this PES as compared to that on the

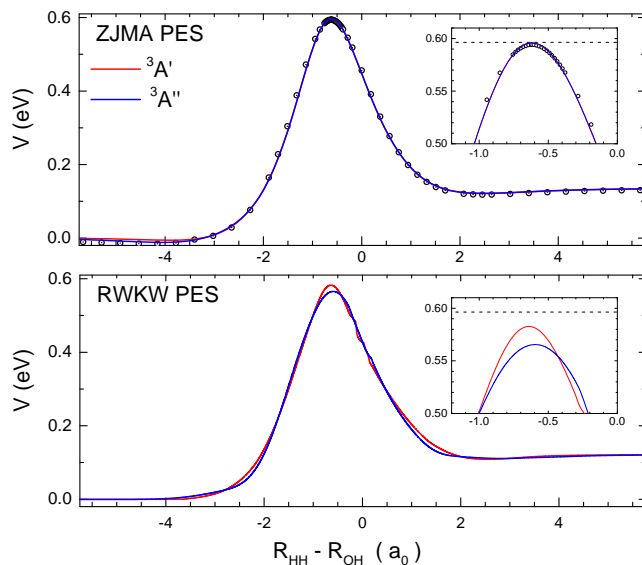


FIG. 4. Minimum energy path in collinear geometry as a function of $R_{\text{HH}}-R_{\text{OH}}$. The top panel corresponds to the current PESs and the bottom panel to the RWKW PESs. As highlighted in the inset, the barrier heights of both PESs of the present work are almost identical and in excellent agreement with the (degenerate) *ab initio* points. At the entrance channel, $R_{\text{HH}} - R_{\text{OH}} < -4 a_0$, where the two states are not degenerate (see Fig. 3), the represented points correspond to the $^3A''$ PES. On the fitted RWKW PESs, in contrast, the differences between the saddle points are evident. To ease the comparison between the two sets of PESs, a horizontal line corresponding to the barrier height for the current $^3A'$ PES is shown in both panels.

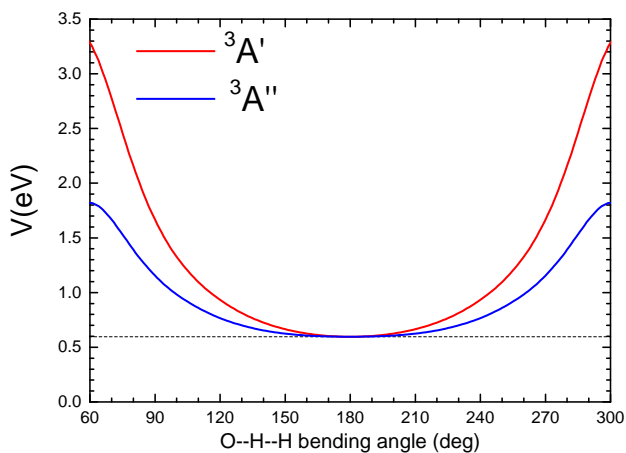


FIG. 5. Potential energy curves of the A' and A'' states as a function of the bending $\widehat{\text{HHO}}$ angle. Each point in the figure correspond to the value of the barrier height for the configuration at a given bending angle.

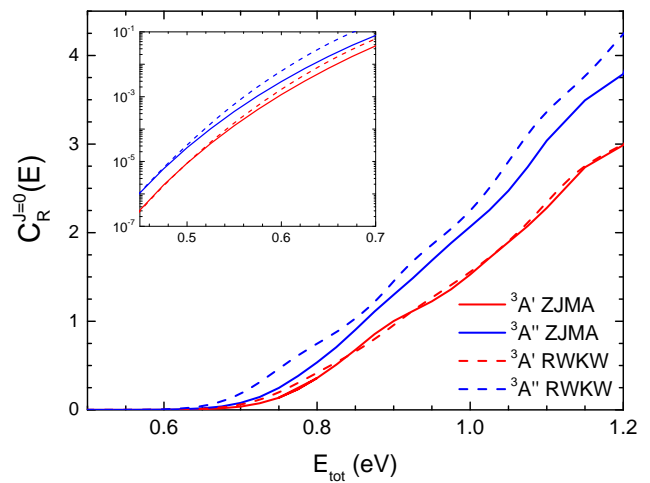


FIG. 6. QM Cumulative Reaction Probabilities calculated for the $^3A'$ (red lines) and $^3A''$ (blue lines) states on the current, ZJMA PESs (solid lines) and the RWKW PESs (dashed lines) for total angular momentum $J=0$.

A'' .

B. Dynamical Results

The cumulative reaction probability^{40–43} (CRP), first employed by Bill Miller in the context of a quantum version of the transition state theory, can be considered as a measure of the number of reactant states that can proceed to products for a given energy. The CRP, which for its convenience is widely used, is one of the most general, and yet accurate, dynamical quantities as it includes the cumulative information for state-to-state processes from every reactant to every product state. Furthermore, it is directly related to the reaction rate coefficient by simply performing the average over the Boltzmann distribution of total energies^{44–50}. Hence, it is a suitable dynamical quantity for comparing the overall reactivity of the two competing $^3A'$ and $^3A''$ PESs involved. It can be used to compare the present with other previous sets of PESs for the same reaction. The QM CRPs for total angular momentum $J=0$, $C_R^{J=0}(E)$, calculated using the present PES (hereinafter ZJMA PES) and the RWKW PESs by Rogers *et al.* are shown in Fig. 6. As expected, based on the evolution of the barrier height with the bending angle, the RWKW and ZJMA A'' PESs are more reactive than their A' counterparts over the whole range of total energies.

As can be seen, regardless of the total energy considered, the RWKW A'' PES is systematically more reactive than the ZJMA A'' PES, while the CRPs for the corresponding A' PESs are fairly similar for total energies above 0.5 eV. At lower energies the reaction probability is basically the same on the two sets of PESs. The lower reaction yield on the ZJMA PESs can be traced back to the respective barrier heights on both sets of PESs; 24

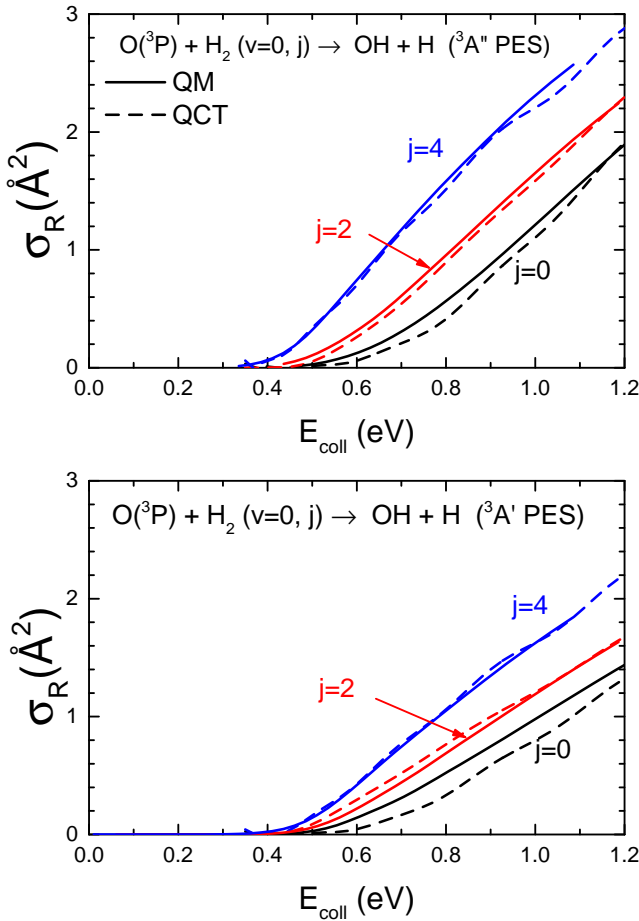


FIG. 7. Comparison between the QCT excitation function, cross section as a function of the collision energy, for the $(^3P) + H_2 (v=0, j)$ reactions on the A'' PES (top panel) and on the A' PES (bottom panel). Results for $j=1$, and 3 (not shown) follow the same trend than their even j counterparts.

meV for the A' and 32 meV for the A'' (see Fig. 4). It should also be stressed that, as expected for reactions characterized by high early barriers, a step-like pattern, associated to the opening of reactant's or products channels, does not show up in any of the CRPs (at the energy necessary to surmount the barrier there are already many open reactant's states). Furthermore, the lack of a resonance pattern suggests that neither the entrance nor the exit Van der Waals wells support bound states.

In what follows we will show only dynamical results calculating using the ZJMA PESs. As already mentioned, the large barrier and unfavorable kinematics for OH detection has impaired experimental measurements for the title reaction. Actually, most of the measurements have been carried out for the collisions between oxygen and deuterium due to its somewhat more favorable kinematics. Relative excitation function was measured for the $O(^3P) + H_2$ reaction using a molecular beam apparatus and a hyperthermal O-atom beam¹⁷ and detection using mass spectrometry.

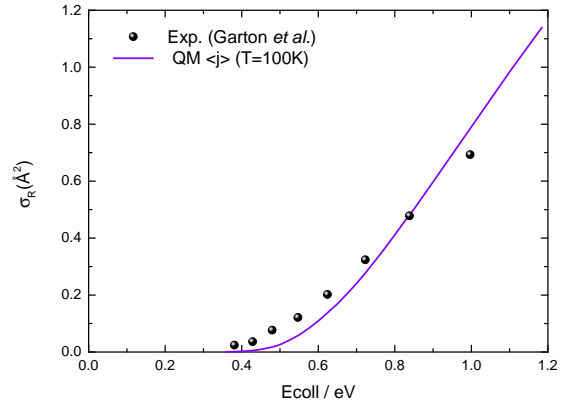


FIG. 8. Comparison between the QM reactive cross sections calculated on the current PESs and those measured by Garton *et al.*¹⁷. See text for more details.

To simulate the experimental excitation function, we have calculated them for different initial rotational states ($j=0-4$) using fully converged QM hyperspherical and QCT methods. The results for $j=0, 2$ and 4 , displayed in Fig. 7, show that regardless of the collision energy considered, H_2 rotation always promotes the reactivity on the two PESs. The agreement between QM and QCT results is fairly good, especially for $j=2$ and 4 , although for $j=0$ the differences are appreciable, the QCT predicting lower cross sections especially on the A' PES. As expected from the previous studies, the cross sections are smaller on the A' than on the A'' PES for all initial rotational states.

To account for the experimental conditions, QM excitation functions calculated on the A' and A'' PES were first averaged according to their statistical factors,

$$\sigma_R(j) = \frac{1}{3} \left(\sigma_R^{A'}(j) + \sigma_R^{A''}(j) \right) \quad (4)$$

and then the excitation functions calculated for the different initial rotational states were averaged according to a 100 K thermal distributions. The results, displayed in Fig. 8, are compared to the experimental excitation function.¹⁷ Since no absolute values were obtained in the cross beam experiments, their absolute values were obtained by scaling the experimental measurements to the QM results. As can be seen, there is a fairly good agreement except at energies close to the threshold, where the present results on the ZMJA results underestimate the reactivity obtained in the experiments. The difference can be in part attributed to contamination with $O(^1D)$ in the beam. In Ref. 17 the authors state that the population of $O(^1D)$ in the beam should be less than a 1%, but reaction between $O(^1D)$ and H_2 has no barrier and even such a small population of $O(^1D)$ could alter the results at very low energies where the reaction yield of $O(^3P)$ with H_2 is practically negligible.

To get a more detailed insight of the comparative reaction dynamics on both PESs, we calculated the evolution of the QM DCS with the collision energy. The reaction

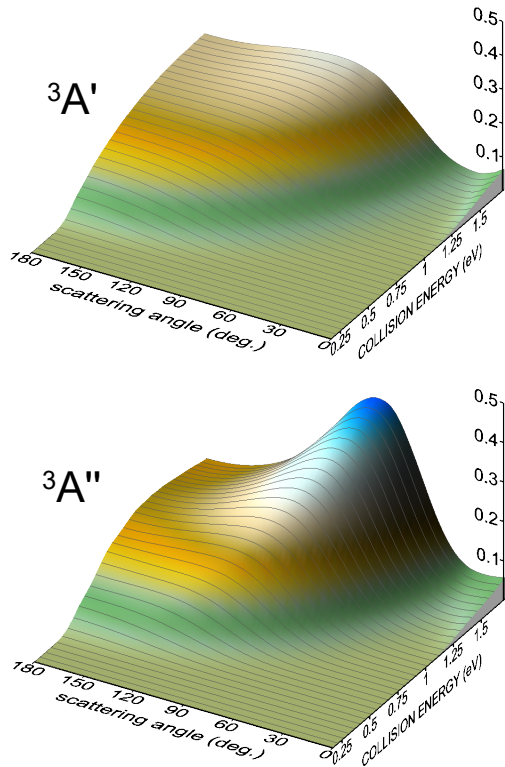


FIG. 9. Reactive DCS as a function of the energy for the $\text{O}(^3\text{P}) + \text{H}_2$ ($v=0, j=1$) collisions on the A'' PES (top panel) and on the A' PES (bottom panel).

with $\text{H}_2(j=1)$ was considered since it is the state that contributes most to the thermal rate coefficient. These results, displayed in Fig. 9, show the different behavior for the non-collinear geometries on the A' and A'' PES causes not only changes in the absolute value, but also the shape of the DCS. At low energies, the DCS on the A' is confined in the backward hemisphere showing a peak at 180° . With increasing collision energies, the peak transforms into a plateau that, at $E_{\text{col}}=1.1$ eV extends to 130° . At $E_{\text{col}} > 1.35$ eV the DCS displays a peak in the forward region and the maximum moves to 100° . The DCS calculated on the A'' covers a wider range of scattering angles. The most salient feature is the shift towards sideways scattering at energies above 1 eV, appearing as a prominent peak at $\theta=90^\circ$ beyond that value. Although the ICS is consistently larger on the A'' PES, the DCS on the A' PES is bigger at backward scattering angles and high collision energies.

The scattering angle-recoil velocity differential cross sections provide a global view of the distribution of internal states as a function of the scattering angle. Figure 10 depicts QM polar maps on the A' (panels a and c) and A'' (panels b and d) PESs for the $\text{O}(^3\text{P})+\text{H}_2(v=0, j=0)$

at 0.83 eV (top panels) and 0.98 eV (bottom panels) collision energies. The main difference between the results on both PESs is the presence of evident sideways scattering of the A'' PES that shifts towards higher angles with increasing energy. By contrast, scattering on the A' is confined to backward angles at the two collision energies shown in Fig. 10. Moreover, the rotational distribution is clearly colder on the A' PES. Not only the maximum of the distribution appears at lower j' values, and hence at larger recoil velocities, but also the rotational distribution is restricted to lower rotational states. As a result of this, the ring corresponding to OH in $v'=1$ is clearly discernable on the A' polar maps, clearly separated from the rotational state rings of $v'=0$. The situation is less clear in the A'' polar maps, as a result of the partial overlap of the highest $v'=0, j'$ states and the lowest j' belonging to the $v'=1$ manifold.

IV. CONCLUSIONS

In this article we have presented a new set of global, analytically fitted PESs for the triple state $\text{O}(^3\text{P}) + \text{H}_2$ reaction. Two adiabatic PESs of symmetries A' and A'' correlating with reactants and products, have been calculated using MRCI and a large basis set. About 5000 *ab initio* points have been calculated for each of the PES and fitted using the GFIT3C procedure. The resulting fits reproduce the *ab initio* potential with great accuracy. In particular, the degeneracy of the transition state region for the O-H-H collinear configuration is reproduced almost exactly. This makes the new set of potential especially suitable for studies aimed at comparing the dynamics on the A' and the A'' PESs. In addition, the long range potential in the entrance channel is also considered, so that these new PESs could also be used to study collisional excitation of H_2 at low temperature.

Quantum mechanical, fully converged, calculations have been performed on both PESs. In good agreement with previous studies, the A'' PES is found considerably more reactive, a behavior that can be traced back to its broader cone of acceptance. Calculations of the excitation functions (collision energy dependence of the reaction cross section) have been carried out for all the rotational states from $j=0$ to $j=4$. A satisfactory agreement has been found in the comparison of the experimental and theoretically simulated excitation functions using the calculations on both PESs weighted over the initial rotational distribution. Differential cross sections (DCSs) as a function of the collision energy are also shown in the present work. The distinct topography of the A' and A'' PESs is reflected in the DCS, which displays a prominent sideways peak on the A'' at energies above 1.0 eV that is absent on the A' PES. In addition, scattering angle-OH recoil velocity polar maps have been calculated at two collision energies to illustrate in a graphical manner the considerable difference in the dynamics of the reaction on each of the PES.

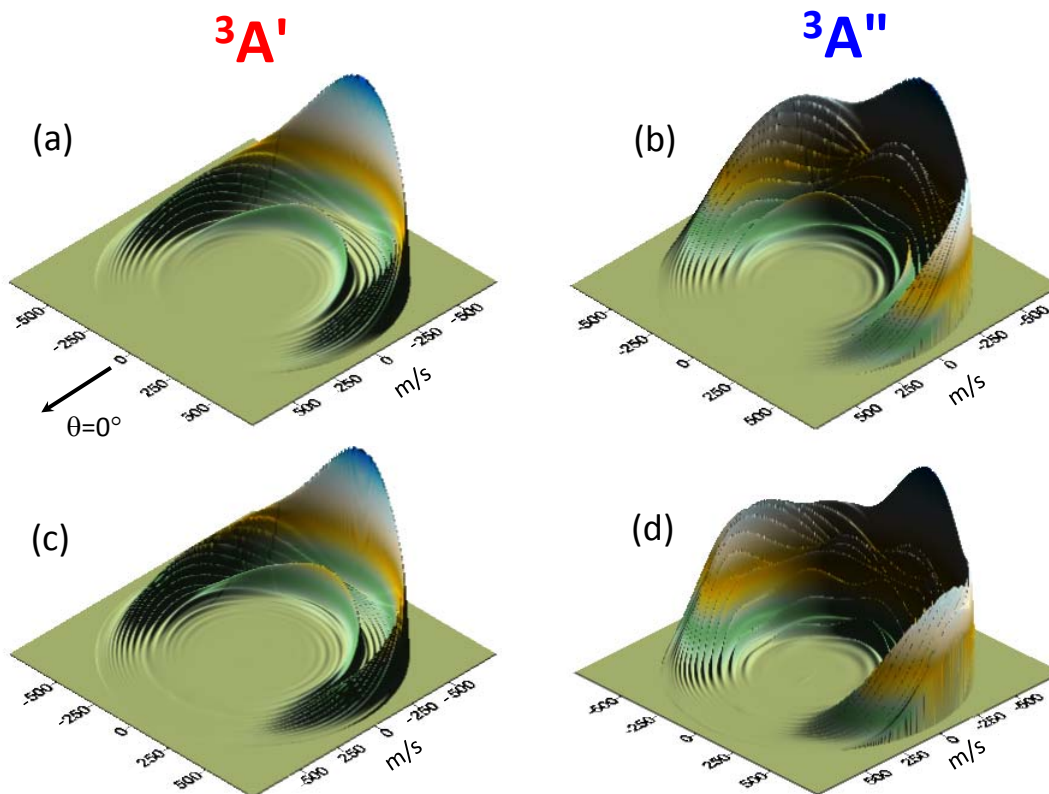


FIG. 10. Scattering angle-OH recoil velocity (ms^{-1}) triple differential cross section (angle-velocity polar maps) at 0.83 eV (panels (a) and (b)) and 0.98 eV (panels (c) and (d)) collision energies. Left and right panels depict the respective polar maps on the A' and A'' PES.

V. ACKNOWLEDGMENT

The authors thank Prof. Enrique Verdasco for his help with the calculations. Funding by the Spanish Ministry of Science and Innovation (grant MINECO/FEDER-CTQ2015-65033-P, and PGC2018-09644-B-100) is also acknowledged. P.G.J. acknowledges funding by Fundación Salamanca City of Culture and Knowledge (programme for attracting scientific talent to Salamanca).

- ¹W. Tsang and R. F. Hampson, J. Phys. Chem. Ref. Data **15**, 1087 (1986).
- ²I. Glassman and R. A. Yetter, *Combustion* (Academic Press, 2008).
- ³L. M. Reynard and D. J. Donaldson, Geophys. Res. Lett. **28**, 2157 (2001).
- ⁴M. M. Graff and A. Dalgarno, Astrophys. J. **317**, 432 (1987).
- ⁵M. Agundez, J. Cernicharo, and J. Goicoechea, Astron. Astrophys. **483**, 831 (2008).
- ⁶T. L. Nguyen and J. F. Stanton, J. Phys. Chem. A **118**, 4918 (2014).
- ⁷J. M. Bowman, Chem. Phys. Lett. **141**, 545 (1987).
- ⁸D. C. Chatfield, R. S. Friedman, G. C. Lynch, D. G. Truhlar, and D. W. Schwenke, J. Chem. Phys. **98**, 342 (1993).
- ⁹S. Rogers, D. Wang, A. Kuppermann, and S. Walsh, J. Phys. Chem. A **104**, 2308 (2000).
- ¹⁰M. R. Hoffmann and G. C. Schatz, J. Chem. Phys. **113**, 9456 (2000).
- ¹¹J. Han, X. Chen, and B. R. Weiner, Chem. Phys. Lett. **332**, 243 (2000).
- ¹²N. Balakrishnan, J. Chem. Phys. **121**, 6346 (2004).
- ¹³P. F. Weck, N. Balakrishnan, J. Brandao, C. Rosa, and W. Wang, J. Chem. Phys. **124**, 074308 (2006).
- ¹⁴J. Zhao, J. Chem. Phys. **138**, 134309 (2013).
- ¹⁵J. Brandao, W. Wang, and C. M. A. Rio, Univ. J. of Chem. **3**, 80 (2015).

- ¹⁶P.-Y. Zhang and L. S-J, Commun. Comput. Chem. **1**, 63 (2015).
- ¹⁷D. J. Garton, T. K. Minton, B. Maiti, D. Troya, and G. C. Schatz, J. Chem. Phys. **118**, 1585 (2003).
- ¹⁸D. J. Garton, A. L. Brunsvold, T. K. Minton, D. Troya, B. Maiti, and G. C. Schatz, J. Phys. Chem. A **110**, 1327 (2006).
- ¹⁹S. A. Lahankar, J. Zhang, K. G. McKendrick, and T. K. Minton, Nat. Chem. **5**, 315 (2013).
- ²⁰S. A. Lahankar, J. Zhang, T. K. Minton, and K. G. McKendrick, J. Am. Chem. Soc. **136**, 12371 (2014).
- ²¹P. G. Jambrina, A. Zanchet, J. Aldegunde, M. Brouard, and F. J. Aoiz, Nat. Comm. **7**, 13439 (2016).
- ²²H.-J. Werner, P. J. Knowles, R. Lindh, M. Schütz, P. Celani, T. Korona, F. R. Manby, G. Rauhut, R. D. Amos, A. Bernhards-son, A. Berning, D. L. Cooper, M. J. O. Deegan, A. J. Dobbyn, F. Eckert, C. Hampel, G. Hetzer, A. W. Lloyd, S. J. McNicholas, W. Meyer, M. E. Mura, A. Nicklass, P. Palmieri, R. Pitzer, U. Schumann, H. Stoll, A. J. Stone, R. Tarroni, T. Thorsteins-son, and M. Wang, "Molpro, version 2012, a package of ab initio programs," See <http://www.molpro.net>.
- ²³H.-J. Werner, P. J. Knowles, G. Knizia, F. R. Manby, and M. Schutz, WIREs Comput. Mol. Sci. **2**, 242 (2012).
- ²⁴T. H. Dunning and Jr., J. Chem. Phys. **90**, 1007 (1989).
- ²⁵H.-J. Werner and P. J. Knowles, J. Chem. Phys. **82**, 5053 (1985).
- ²⁶H.-J. Werner, B. Follmeg, and M. H. Alexander, J. Chem. Phys. **89**, 3139 (1988).
- ²⁷E. R. Davidson, J. Comp. Phys. **17**, 87 (1975).
- ²⁸A. Aguado and M. Paniagua, J. Chem. Phys. **96**, 1265 (1992).
- ²⁹A. Aguado, C. Suarez, and M. Paniagua, J. Chem. Phys. **98**, 308 (1993).
- ³⁰A. Aguado, C. Tablero, and M. Paniagua, Comput. Phys. Com-mun. **108**, 259 (1998).
- ³¹R. Rydberg, Z. Phys. **73**, 25 (1931).
- ³²A. Zanchet, O. Roncero, S. Omar, M. Paniagua, and A. Aguado, J. Chem. Phys. **132**, 034301 (2010).
- ³³A. Dorta-Urra, A. Zanchet, O. Roncero, A. Aguado, and P. B. Armentrout, J. Chem. Phys. **135**, 091102 (2011).
- ³⁴A. Zanchet, M. Agúndez, V. J. Herrero, A. Aguado, and O. Ron-cero, Astron. J. **146**, 125 (2013).
- ³⁵A. Dorta-Urra, A. Zanchet, O. Roncero, and A. Aguado, J. Chem. Phys. **142**, 154301 (2015).
- ³⁶D. Skouteris, J. F. Castillo, and D. E. Manolopoulos, Comp. Phys. Comm. **133**, 128 (2000).
- ³⁷F. J. Aoiz, L. Bañares, and V. J. Herrero, J. Chem. Soc. Faraday. Trans. **94**, 2483 (1998).
- ³⁸F. J. Aoiz, V. J. Herrero, and V. Sáez-Rábanos, J. Chem. Phys. **97**, 7423 (1992).
- ³⁹K. P. Huber and G. Herzberg, *Molecular Spectra And Molecu-lar Structure, IV. Constants Of Diatomic Molecules* (Springer Science + Business Media, LLC, 1979).
- ⁴⁰W. H. Miller, J. Chem. Phys. **62**, 1899 (1975).
- ⁴¹W. H. Miller, J. Chem. Phys. **65**, 2216 (1976).
- ⁴²W. H. Miller, Acc. Chem. Res. **9**, 306 (1976).
- ⁴³W. H. Miller, Acc. Chem. Res. **26**, 174 (1993).
- ⁴⁴D. C. Chatfield, R. S. Friedman, D. G. Truhlar, B. C. Garrett, and D. W. Schwenke, J. Am. Chem. Soc. **113**, 486 (1991).
- ⁴⁵D. C. Chatfield, R. S. Friedman, D. G. Truhlar, B. C. Gar-rett, and D. W. Schwenke, Faraday Discuss. Chem. Soc. **91**, 289 (1991).
- ⁴⁶D. C. Chatfield, Firdman, D. W. Schwenke, and D. G. Truhlar, J. Phys. Chem. **96**, 2414 (1992).
- ⁴⁷P. G. Jambrina, F. J. Aoiz, C. J. Eyles, V. J. Herrero, and V. Sáez-Rábanos, J. Chem. Phys. **130**, 184303 (2009).
- ⁴⁸P. G. Jambrina, M. Lara, M. Menéndez, J.-M. Launay, and F. J. Aoiz, J. Chem. Phys. **137**, 164314 (2012).
- ⁴⁹F. J. Aoiz, V. J. Herrero, and V. Sáez-Rábanos, J. Chem. Phys. **129**, 024305 (2008).
- ⁵⁰F. J. Aoiz, V. J. Herrero, M. P. de Miranda, and V. Sáez-Rábanos, Phys. Chem. Chem. Phys. **9**, 5367 (2007).